Particle-based mesoscopic model for phase separation in a binary fluid mixture

Surabhi Jaiswal,[1] Soudamini Sahoo,[2] and Snigdha Thakur[1,*]

[1]*Department of Physics, Indian Institute of Science Education and Research Bhopal, Madhya Pradesh 462066, India*

[2]*Department of Physics, Indian Institute of Technology Palakkad, Kerala 678623, India*

(Received 12 December 2022; accepted 20 April 2023; published 10 May 2023)

A mesoscopic simulation model to study the phase separation in a binary fluid mixture in three dimensions (3D) is presented here by augmenting the existing particle-based multiparticle collision dynamics (MPCD) algorithm. The approach describes the nonideal equation of the fluid state by incorporating the excluded-volume interaction between the two components within the framework of stochastic collision, which depends on the local fluid composition and velocity. Calculating the nonideal contribution to the pressure both from simulation and analytics shows the model to be thermodynamically consistent. A phase diagram to explore the range of parameters that give rise to phase separation in the model is investigated. The interfacial width and phase growth obtained from the model agree with the literature for a wide range of temperatures and parameters.

DOI: 10.1103/PhysRevE.107.055303

I. INTRODUCTION

Phase separation is ubiquitous at various lengths and time scales in nature. For example, the biomolecular condensates in cell biology where the process of phase separation forms the membrane-less organelles to regulate different biological activities [1,2], protein solutions where a network structure of the protein-rich phase is formed, giving rise to the viscoelastic effect [3,4], colloidal systems [5,6], oil-water mixture [7], etc. The phase separation process strongly depends on the surrounding ambience and is a complex procedure. To understand the associated phenomena, many theoretical [8,9] and experimental [10,11] avenues have been established. These studies have many practical applications like waste water treatment, protein purification, polymer films, chemical analysis, etc. [11–13].

Because of the complexity of the process, simulations have played an essential role in understanding many of the experimental observations on the phase-separating systems [14,15]. The fact that phase separation involves multiphase flow and is observed at varied lengths and time scales demands the need for coarse-grained mesoscale simulation techniques having the ability to incorporate thermal fluctuations and hydrodynamics. A few popular techniques in this regard are the lattice Boltzmann method (LBM) [16,17], dissipative particle dynamics (DPD) [18,19], and multiparticle collision dynamics (MPCD) [20,21]. The initial LBM methods to incorporate multicomponent flow had the limitation on the interactions between the particles to achieve thermodynamic consistencies [21,22], which was then addressed by Yeomans in the case of binary fluid mixtures [17]. The implementation of multicomponent fluid in the framework of DPD is rather straightforward [23], however, it is computationally more expensive than its counterparts. Among all the existing coarse-grained simulation methods, multiparticle collision dynamics (MPCD) has proven to be one of the most popular methods due to its simplicity and versatility. This has led to its application in systems ranging from colloids [24,25], polymers [26,27], proteins [28], and vesicles [29,30] to viscoelastic fluids [31]. The self-propulsion and active matter field has also been extensively explored using MPCD [32,33]. Researchers are trying to build different forms of MPCD to model multiphase flows [20,21,34–37], which can then be applied to a variety of problems consisting of colloids and polymers in phase separating medium [38–40].

It is important to note that the MPCD simulation scheme was initially designed using the ideal gas equation [41], therefore, the original form of MPCD is not appropriate for simulating the phase separation in the binary or ternary fluids. Two major approaches have been identified in the literature to overcome this challenge and to introduce the nonideal equation of state. In one, a free-energy-based MPCD method has been developed in line with LBM [21]. While the second approach consists of modifying the MPCD algorithm to model excluded volume effects so that the nonideal equation of state can be achieved [20,34,35]. The second approach is however limited to mostly the two-dimensional binary and ternary systems. In this work, we have developed a coarse-grained simulation model by modifying MPCD for a phase separating binary fluid mixture in three dimensions (3D). We consider the repulsive interactions among the different species to incorporate the nonideal equation of state, which is similar to the approach taken by Ihle *et al.* in two dimensions (2D) [20,35]. The model developed here preserves the average phase-space volume and the local mass, momentum, and energy of the system. Further, it achieves phase separation even at higher temperatures, which was the limitation of the previous work [20]. We have witnessed a percolating or connected morphology for the critical mixture and droplet morphology for the off-critical mixture. The phase diagram explores the range of model parameters and temperature to obtain the phase

*sthakur@iiserb.ac.in

separation for our model. Further, we identify the parameter values suitable for the model to be thermodynamically consistent by comparing the pressure from simulation and analytic calculation. The phase separation and phase growth are characterized by calculating the interfacial width and domain size coarsening.

The organisation of the work is as follows: Section II elucidates our simulation model for phase separation of a binary mixture using a modified multiparticle collision method. Section III describes the results in terms of the probability distribution of order parameter, phase diagram, pressure calculation, interfacial stability analysis, and domain coarsening. Section IV concludes the work and provides the future direction.

II. SIMULATION MODEL

The multiparticle collision dynamics (MPCD) [41] is a simplified coarse-grained mesoscopic model that retains all the essential features of molecular dynamics [25]. Historically, it was developed for single-component solvents to accomplish explicit solvent simulations costeffectively. Recently, a few modifications in MPCD have been carried out to model binary fluid mixtures [20,34]. As stated before, this work tries to model a phase separating binary mixture in three dimensions. Our model considers a binary fluid mixture of "A" type particles with number density ρ_A and "B" type particles with number density ρ_B in three dimensions. Phase separation in a binary mixture can be obtained by implementing attraction among the same species of particle and/or repulsion between two different species [42,43]. We introduce an effective repulsion between "*A*" and "*B*" particles to induce phase separation. We have extended the technique adapted by Ihle *et al.* [35,44,45] that was focused on two-dimensional systems by considering the nonideal equation of state.

The MPCD consists of two steps: streaming and collision steps. In the streaming step, the positions of all the solvent particles are updated by following Newton's equation of motion as

$$\mathbf{r}_i(t+\tau) = \mathbf{r}_i(t) + \mathbf{v}_i(t)\tau, \tag{1}$$

where $\mathbf{r}_i(t)$ and $\mathbf{v}_i(t)$ are the position and velocity of the ith particle at time t, respectively. For the regular MPCD, the exchange of momentum (collision) is performed at a time interval of τ within cubical cells of size a. The modification in the regular MPCD is carried out to introduce phase separation. Instead of performing the collision in a single cell, we introduce a "supercell" of length $2a$, which consists of eight adjacent cubical cells. In every supercell, a pair of cells is selected randomly to perform a collision. There are 13 possible directions [46] for selecting a cell pair from a supercell, which are listed in Table I, and the representative figure for few directions are shown in Fig 1. These are (i) three 1D collision directions $\boldsymbol{\sigma}_1$ to $\boldsymbol{\sigma}_3$, (ii) six 2D collision directions $\boldsymbol{\sigma}_4$ to $\boldsymbol{\sigma}_9$, and (iii) four 3D collision directions $\boldsymbol{\sigma}_{10}$ to $\boldsymbol{\sigma}_{13}$. The probability of choosing each of these collision directions is considered to be equal ($=\frac{1}{13}$), to ensure that there is no biasing of collision or fluid flow in any direction, hence the isotropy in the system.

TABLE I. Possible choices of directions for selecting a cell pair from a supercell to perform collisions.

$\boldsymbol{\sigma}_1$	$\boldsymbol{\sigma}_2$	$\boldsymbol{\sigma}_3$	$\boldsymbol{\sigma}_4$	$\boldsymbol{\sigma}_5$	$\boldsymbol{\sigma}_6$	$\boldsymbol{\sigma}_7$	$\boldsymbol{\sigma}_8$
$\hat{x}$	$\hat{y}$	$\hat{z}$	$\frac{\hat{x}+\hat{y}}{\sqrt{2}}$	$\frac{\hat{x}-\hat{y}}{\sqrt{2}}$	$\frac{\hat{x}+\hat{z}}{\sqrt{2}}$	$\frac{\hat{x}-\hat{z}}{\sqrt{2}}$	$\frac{\hat{y}+\hat{z}}{\sqrt{2}}$

$\boldsymbol{\sigma}_9$	$\boldsymbol{\sigma}_{10}$	$\boldsymbol{\sigma}_{11}$	$\boldsymbol{\sigma}_{12}$	$\boldsymbol{\sigma}_{13}$
$\frac{\hat{y}-\hat{z}}{\sqrt{2}}$	$\frac{\hat{x}+\hat{y}+\hat{z}}{\sqrt{3}}$	$\frac{\hat{x}-\hat{y}+\hat{z}}{\sqrt{3}}$	$\frac{\hat{x}+\hat{y}-\hat{z}}{\sqrt{3}}$	$\frac{\hat{x}-\hat{y}-\hat{z}}{\sqrt{3}}$

The collision between two species can occur either by all the A particles from the first cell undergoing a collision with all the B particles in the second cell or vice versa. Let us consider all the A particles in the first cell having $\mathbf{v}_A = (\Sigma_{i=1}^{N_A}\mathbf{v}_i)/N_A$ as their mean velocity collide with all the B particles in the second cell having $\mathbf{v}_B = (\Sigma_{i=1}^{N_B}\mathbf{v}_i)/N_B$ as the mean velocity.

To find the collision probability we define a quantity $\Delta v_{AB} = \boldsymbol{\sigma}_j \cdot (\mathbf{v}_A - \mathbf{v}_B)$, where Δv_{AB} is the projection of the difference of the mean velocities of selected cell pairs on the collision direction $\boldsymbol{\sigma}_j$. This collision rule is in accordance with the hard-sphere collision, wherein, if $\Delta v_{AB} > 0$ then all A particles in the first cell will collide with all B particles in the second cell with the following acceptance probability [34,45]:

$$P_A(N_A, N_B, \Delta v_{AB}) = \min(1, \alpha N_A N_B \Delta v_{AB}\Theta(\Delta v_{AB})), \tag{2}$$

where $\Theta(\Delta v_{AB})$ is the unit step function and "α" is the repulsive parameter. The above acceptance probability with the appropriate choice of α (will be discussed later) ensures the thermodynamic consistency of the model [20,45]. If $\Delta v_{AB} < 0$, then there will not be any collision. As done before, to reduce the compressibility effect and to get a high speed of sound, we consider only the parallel or longitudinal

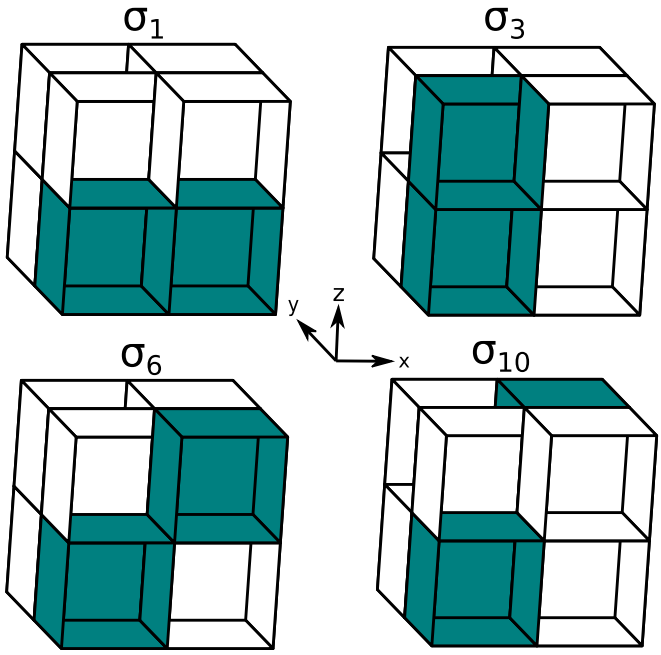

FIG. 1. Schematic of supercell for selecting a cell pair in a given direction for collision.

component of the momentum transfer (component parallel to σ_j) [44]. After the collision, the parallel components of mean velocities of colliding particles in the two cells are given by the equation

$$\mathbf{v}_i^{||}(t+\tau_{AB}) - \mathbf{v}_{AB}^{||} = -(\mathbf{v}_i^{||}(t) - \mathbf{v}_{AB}^{||}), \tag{3}$$

where $\mathbf{v}_{AB}^{||} = \frac{(\mathbf{v}_A^{||}N_A + \mathbf{v}_B^{||}N_B)}{(N_A+N_B)}$ is the parallel component of the mean velocities of colliding particles. This conserves momentum and energy in the cell pairs. The perpendicular component will be the same as before the collision. Similarly, the collision between all B particles in the first cell with all the A particles in the second cell can be performed.

In addition to the A-B collision, we perform the A-A and B-B collisions to incorporate all possible interactions in the fluid, hence, crucial for mixing the particle momenta. All the A-A and B-B interactions are taken care of by the usual collision rule of MPCD, wherein the velocity of all the solvent particles in the single cell is rotated with respect to the center of mass about a randomly selected axis [41]:

$$\mathbf{v}_{i,\beta}(t+\tau_c) = \mathbf{v}_{cm,\beta}(t) + \omega(\phi)(\mathbf{v}_{i,\beta}(t) - \mathbf{v}_{cm,\beta}(t)), \tag{4}$$

where $\omega(\phi)$ is the rotation with an angle ϕ around the randomly chosen axis and $\mathbf{v}_{cm,\beta}(t)$ is the center of mass velocity of species β (A or B) at time t. The same random vector with components in the range $[-a, a]$ is used to shift every particle prior to the collision, maintaining Galilean invariance [47]. Following the collision, all particles are moved back by the same amount. Note that one may choose two different values of τ_c for the A-A and B-B collision to model a binary fluid with components having different viscosities.

Simulation Parameters: All the lengths are measured in terms of a. We have chosen $a = 1$ and mass of solvent particles, $m = 1$. Unless otherwise specified, the length of the simulation box is taken as $L_x = L_y = L_z = 32\,a$. The density of the bulk fluid is kept fixed as $\rho = \rho_A + \rho_B = 10.0$ with ρ_A and ρ_B as the density of A and B particles, respectively. The temperature has been varied between $k_BT = 0.006$ to 0.09 and the repulsion parameter α is varied between 0.0 to 0.24. The MPCD simulation time steps and the rotation angle are taken to be $\tau = 0.01$, $\tau_{AB} = 10 \times \tau$, $\tau_c = 50 \times \tau$, and $\phi = \frac{\pi}{2}$, respectively. In principle, one can take $\tau_{AB} = \tau_c$, then the values of the repulsion parameter α to attain phase separation will be different from the values reported here.

III. RESULTS

Phase separation is not an instantaneous process; Instead, it is a complex process that involves the influence of various quantities like density, interparticle interaction, temperature, external perturbations, etc. Here, our aim is to explore the effects of temperature (k_BT) and repulsive parameters (α) on the phase separation process by quantifying it through order parameter, solvent density profile, interfacial width, and domain growth in our proposed 3D mesoscopic model.

A. Order parameter and phase diagram

When a homogeneous binary mixture is quenched below the critical temperature, the mixture becomes unstable with respect to small perturbations and move toward a phase-separated equilibrium state. Depending on the density of different components and temperature, phase separation usually proceeds through spinodal decomposition or nucleation. The domain formation and its growth along with its morphology depends upon various factors including density, hydrodynamics, and temperature of the system [9,48,49].

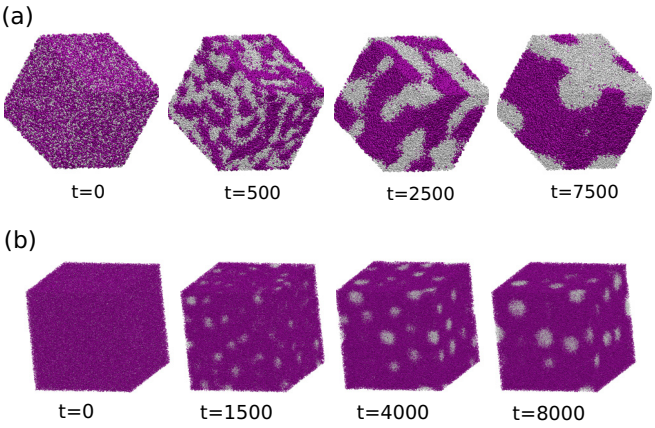

FIG. 2. Snapshots captured during the phase evolution of a binary mixture from a homogeneous state to a phase-separated state. A and B particles are shown in white and purple color, respectively. Simulation times are mentioned below the snapshots. (a) A critical (or symmetric) binary mixture ($\rho_A = \rho_B = 5$). (b) An off-critical (or asymmetric) binary mixture ($\rho_A = 1$ and $\rho_B = 9$). Simulation box size is $48a \times 48a \times 48a$, $k_BT = 0.006$ and $\alpha = 0.2$.

Using our simulation approach, we observe the phase separation process in both critical (or symmetric) and off-critical (or asymmetric) binary fluid mixtures, quenched at a temperature much below the critical temperature. The evolution from an unstable critical mixture ($\rho_A = \rho_B = 5$) toward a stable phase separated state, owing to the minimization of energy is quite clear from Fig. 2(a). Typically, when the system is quenched from the metastable region, the phase separation proceeds through nucleation. For off-critical binary fluid, we consider the fluid density of different species as $\rho_A = 1$ and $\rho_B = 9$. Formation of small droplets at early time and their growth mostly through diffusion can be seen from Fig. 2(b). At the late times, we observe the droplets of A rich particles in the background of the B rich phase, as $\rho_A < \rho_B$. Hence, the model effectively proves that it can produce the connected and droplet morphologies for critical and off-critical binary mixtures, respectively.

To check the transport properties of our model we calculated the self-diffusion coefficient of β (A or B) species by calculating the mean-square displacement. The self-diffusion coefficient of species β is defined as

$$D_\beta = \lim_{t\to\infty} \frac{\langle[\mathbf{r}_\beta(t) - \mathbf{r}_\beta(0)]^2\rangle}{2dt}, \tag{5}$$

where $d = 3$ is the dimension of the system and $\mathbf{r}_\beta$ is the position of particles with species β. The average is being done over all the particles of the species. Figure 3 represents the values of the self-diffusion coefficient (D_β) with respect to temperature calculated from simulations. This suggests that

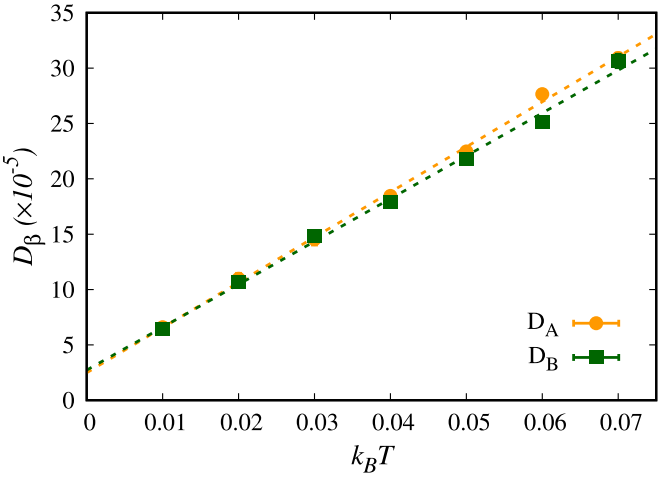

FIG. 3. Self-diffusion coefficient of species β with respect to temperature for $\alpha = 0.2$.

the self-diffusion coefficient is following a linear response with respect to temperature. We have also calculated the viscosity of the system from simulation which is defined as the correlation of the xy component of the stress tensor given as [35,50]

$$\eta = \frac{\tau_c}{(N_A + N_B)k_BT} \sum_{q=0}^{\infty} \langle T_{xy}(0) T_{xy}(q\tau_c) \rangle, \tag{6}$$

where $T_{xy}(0)$ is the stress tensor at time $t = 0$ and $T_{xy} = T_{xy}^{\text{kin}} + T_{xy}^{\text{col}}$, where T_{xy}^{kin} and T_{xy}^{col} are the kinetic and collisional contributions to the viscosity respectively. They are defined as [50]

$$T_{xy}^{\text{kin}}(q\tau_c) = -\sum_i v_{ix}(q\tau_c) v_{iy}(q\tau_c), \tag{7}$$

$$T_{xy}^{\text{col}}(q\tau_c) = -\frac{1}{\tau_c} \sum_i S_{iy}(q\tau_c) v_{ix}(q\tau_c), \tag{8}$$

where $S_{iy}(q\tau_c) = \zeta_{iy}^s((q+1)\tau_c) - \zeta_{iy}^s(q\tau_c) - \tau v_{iy}(q\tau_c)$. Here $\zeta_{iy}^s(q\tau_c)$ is the y cell coordinate of the ith particle at time $(q\tau_c)$ after shifting the grid, where q is an integer. With the above, the kinematic viscosity (η/ρ) for $k_BT = 0.01$ is found to be $\approx$2.0.

Further, we investigate the effect of temperature on the phase separation by calculating the probability distribution of the normalized order parameter, which is defined in the jth cell as

$$\psi_\beta^j = \frac{(\rho_\beta^j - \rho_{\beta^*}^j)}{\rho}, \tag{9}$$

where β and β^* represent the two different solvent species. ρ_β^j is the density of species β $(= A$ or $B)$ in the jth cell, and ρ is the bulk solvent density. If $\beta = A$ and $\beta^* = B$ then $\psi_\beta^j > 0$ in a cell represents A rich phase, $\psi_\beta^j < 0$ represents B rich phase, and $\psi_\beta^j = 0$ represents a mixed state. Figure 4 shows the probability distribution of the normalized order parameter ψ_β^j. The distribution has two peaks for temperature $k_BT = 0.005$, and for temperature $k_BT = 0.09$, a single peak is observed. Two peaks at lower temperatures represent two

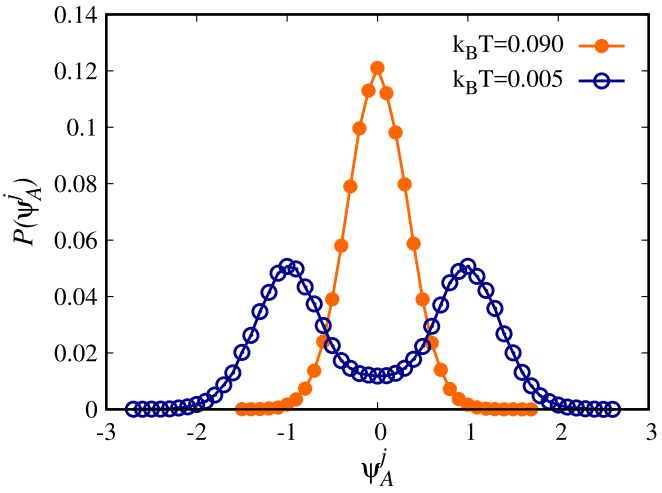

FIG. 4. The probability distribution of the normalized order parameter ψ_A^j for two different temperatures $k_BT = 0.005$ and 0.090 with $\alpha = 0.2$.

coexisting A rich and B rich phases, whereas the single peak at higher temperatures represents a mixed phase.

In addition to the fluid density and temperature, interaction among fluid particles also plays a vital role in phase separation. We explore a range of temperature and repulsive parameters for the symmetric binary mixture to determine the span of these parameters to observe phase separation. We quantify the phase separation by absolute order parameter $\tilde{\psi}$, defined as

$$\tilde{\psi} = \frac{1}{N_\chi} \sum_{j=1}^{N_\chi} \langle |\psi_\beta^j| \rangle, \tag{10}$$

where N_χ is the total number of cells. The symbol $\langle .. \rangle$ is meant for the time and ensemble average. Figure 5 plots the $\tilde{\psi}$, which decides the phase state. $\tilde{\psi} \approx 0$ identifies the range of parameters that result in a mixed phase, and $\tilde{\psi} \approx 1$ provides the set of parameters that represent a phase-separated state. It is clear from Fig. 5 that for $k_BT \leqslant 0.06$ and $\alpha \geqslant 0.12$ the equilibrium state of the system is a phase-separated state. For

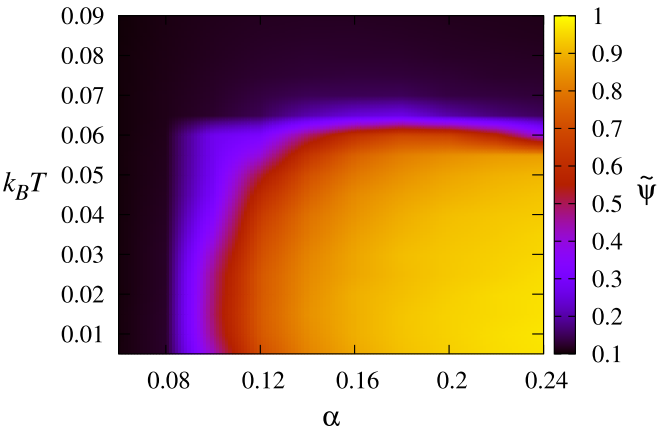

FIG. 5. The phase diagram for the absolute order parameter with respect to temperature k_BT and the repulsive parameter α.

higher temperatures, the system stays in a mixed state (the black-colored region in the phase diagram), irrespective of the repulsive parameter α. Therefore, the above phase diagram suggests that the proposed model works for a large combination of temperature and repulsive parameters to yield phase separation.

B. Pressure calculation

The model mimics phase separation with hard sphere collisions and there is no explicit potential energy in the system. Therefore, the nonideal contribution to the pressure is expected to behave linearly with temperature in order to verify the model's thermodynamic consistency [44,45]. To understand the pressure behavior for α and k_BT, we conduct the analytical analysis and match this with the calculated pressure from the simulation. Since the nonideal contribution in our model comes from the *A*-*B* collision between the double cells, we focus on the momentum transport through a fixed surface during the *A*-*B* collision.

To find the analytical expression of pressure in a 3D binary fluid system, we follow the analysis of 2D binary systems [35,44]. Following the symmetry along any Cartesian axis in our cubical simulation box, the pressure tensor's x, y, and z components will be identical. Therefore, we focus on the x component of pressure tensor, i.e., P_{xx}. Out of the 13 possible directions given in Table I, the double cells aligned along the directions $\boldsymbol{\sigma}_1, \boldsymbol{\sigma}_4, \boldsymbol{\sigma}_5, \boldsymbol{\sigma}_6, \boldsymbol{\sigma}_7, \boldsymbol{\sigma}_{10}, \boldsymbol{\sigma}_{11}, \boldsymbol{\sigma}_{12}$, and $\boldsymbol{\sigma}_{13}$ will contribute to P_{xx}.

As discussed in the model section, the collision is performed in homogeneously shifted double cells. The distance δx between the left most corner of a double cell and the dividing plane in x direction is distributed homogeneously from $x = 0$ to $x = 2a$. Let g_x be the momentum transfer through the plane at $\delta x = x$. $g_x = g_m$ is the momentum transfer through the dividing plane which passes through the center of the double cell, i.e., at $\delta x = a$ and depends on the direction of collision, i.e., σ_j. The average momentum transfer through this dividing plane is zero at $\delta x = 0$ and $\delta x = 2a$, and increases linearly with a maximum at $\delta x = a$. So we can write $g_x = \frac{g_m}{a}x$ for $0 \leqslant x \leqslant a$. Now doing the position average over the planes at $\delta x = x$ gives us the average momentum transfer $\bar{g}$ as

$$\bar{g} = \frac{\int_0^a \int_0^a \int_0^a g_x dx dy dz}{\int_0^a \int_0^a \int_0^a dx dy dz} = \frac{g_m}{2}. \tag{11}$$

To calculate P_{xx}, we start with the collision along the horizontal double cells $\boldsymbol{\sigma}_1$ direction. Let the N_A number of A particles in the left cell collide with the N_B number of B particles in the right cell. Then the x component of the change in momentum undergoing a collision in the left cell is given as

$$\begin{aligned}\Delta g_x &= m \sum_{i=1}^{N_A} [\mathrm{v}_{ix}(t + \tau_{AB}) - \mathrm{v}_{ix}(t)] \\ &= -2\,\mu_m\,\Delta v_{ABx}.\end{aligned} \tag{12}$$

Here $\mathrm{v}_{ix}(t + \tau_{AB}) = 2v_{ABx} - \mathrm{v}_{ix}(t)$ is the x component of the velocity of particles after the collision and v_{ABx} is the x component of center of mass velocity of the double cell. $\Delta v_{ABx} = v_{AB1x} - v_{AB2x}$ is the difference in the mean velocities of particles in the left and right cell, and $\mu_m = m\frac{N_A N_B}{N_A + N_B}$ can be considered as reduced mass.

Assuming the same number of particles in left and right cells, the thermal average momentum transfer across the surface is

$$\langle g_x \rangle = \frac{w}{2} \int_0^\infty P_A(N_A, N_B, \Delta v_{ABx})\, p(\Delta v_{ABx})\, \Delta g_x\, d(\Delta v_{ABx}). \tag{13}$$

The factor $\frac{1}{2}$ comes from the position average of the dividing planes as discussed in Eq. (11). $P_A(N_A, N_B, \Delta v_{ABx})$ is the acceptance probability of the collision and w is the probability of having a collision in the σ_1 direction. $p(\Delta v_{ABx})$ is the probability of getting micro-state Δv_{ABx}, and is assumed to follow the Maxwell-Boltzmann distribution,

$$p(\Delta v_{ABx}) = \left(\frac{\mu_m}{2\pi k_B T}\right)^{\frac{1}{2}} \exp\left(-\frac{\mu_m (\Delta v_{ABx})^2}{2k_B T}\right). \tag{14}$$

Using Eqs. (2), (12), and (14) in Eq. (13), P_{xx} because of horizontal collision in $\boldsymbol{\sigma}_1$ direction can be given as

$$P_1 = \frac{\langle g_x \rangle}{\tau_{AB}\, a^2} = -\frac{w\,\alpha\, N_A\, N_B\, k_B T}{2\,\tau_{AB}\, a^2}, \tag{15}$$

where a^2 is the area of the plane, normal to the σ_1 direction.

Following the similar strategy, next we calculate the contribution to the pressure P_{xx} due to the collisions along the face-diagonal directions ($\boldsymbol{\sigma}_4, \boldsymbol{\sigma}_5, \boldsymbol{\sigma}_6$, and $\boldsymbol{\sigma}_7$). The total momentum transfer due to these four collision directions is $\Delta g_x = -4\,\mu_m\,\Delta v_{ABx}$, and the pressure due to these collisions is

$$P_2 = \frac{\langle g_x \rangle}{\tau_{AB}\sqrt{2}\, a^2} = -\frac{w_{fd}\,\alpha\, N_A\, N_B\, k_B T}{\tau_{AB}\,\sqrt{2}\, a^2}, \tag{16}$$

where w_{fd} is the probability of collision in the face diagonal direction and $\sqrt{2}\,a^2$ is the area normal to the plane.

The remaining contribution to the pressure P_{xx} comes from the collision along the body diagonal ($\boldsymbol{\sigma}_{10}, \boldsymbol{\sigma}_{11}, \boldsymbol{\sigma}_{12}$, and $\boldsymbol{\sigma}_{13}$). The total momentum transfer due to these collisions is $\Delta g_x = -\frac{8}{3}\,\mu_m\,\Delta v_{ABx}$, and the pressure due to these is given as

$$P_3 = \frac{\langle g_x \rangle}{\tau_{AB}\left(\frac{3\sqrt{3}a^2}{2}\right)} = -\frac{4}{9\sqrt{3}}\frac{w_{bd}\,\alpha\, N_A\, N_B\, k_B T}{\tau_{AB}\, a^2}, \tag{17}$$

where w_{bd} is the probability of collision in the body diagonal direction and the area of the plane crossed by the particles for collision is $\frac{3\sqrt{3}a^2}{2}$.

From Eqs. (15)–(17), the final expression for the total pressure P_{xx} (considering the magnitude) can be written as

$$\begin{aligned}P &= P_1 + P_2 + P_3 \\ &= \left(w + \sqrt{2}\,w_{fd} + \frac{8}{9\sqrt{3}}\,w_{bd}\right)\frac{\alpha\, N_A\, N_B\, k_B T}{2\,\tau_{AB}\, a^2}.\end{aligned} \tag{18}$$

Based on the selected directions, $w = 1/13$, $w_{fd} = 4/13$, and $w_{bd} = 4/13$.

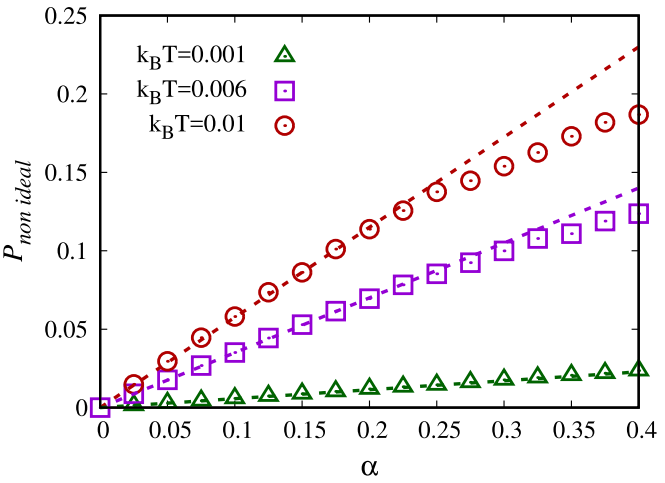

FIG. 6. Figure shows the variation of nonideal pressure as a function of α for different temperatures $k_BT = 0.001, 0.006$, and 0.01 which are found by simulation using Eq. (19). The symbols correspond to the simulations and the dotted lines are the linear fit considering small α values.

To validate our model, we simulate the pressure from the ensemble average of the diagonal components of the microscopic stress tensor and compare it with the analytical expression derived in Eq. (18). The x component of the pressure from the simulation is given as [35,44]

$$P = P_{\text{ideal}} + P_{\text{non ideal}} = \frac{1}{\tau_{AB}V}\left\langle \sum_{j=1}^{N_\chi}\sum_{i\in j}\left[\tau_{AB}\mathrm{v}_{ix}^2 - \frac{\Delta \mathrm{v}_{ix} z_{ikx}}{2}\right]\right\rangle, \tag{19}$$

where N_χ represents total number of cells, $\Delta \mathrm{v}_{ix}(t) = \mathrm{v}_{ix}(t + \tau_{AB}) - \mathrm{v}_{ix}(t)$. z_{ikx} represents the index of pair of cells involved in the collision event at time τ_{AB}, and k represents the index of the selected direction σ_k. z_{ikx} can have values -1, 0, and 1 depending on the cell coordinates [20,35]. The first term in Eq. (19) represents the ideal contribution while the second term represents the nonideal contribution to the pressure.

As stated before, for the model to be thermodynamically consistent, the pressure varies linearly with temperature for a given choice of repulsive parameter. Figure 6 shows our simulation result for the variation of nonideal pressure with respect to the repulsive parameter (α), and the dotted lines are the linear fits to the simulation data points. The slope calculated from this linear fit is compared with the slope obtained from our analytical result in Table II. The fact that these two are in good agreement with each other substantiates our $3D$ model for binary fluid phase separation for thermodynamical consistency. Furthermore, as evident from Fig. 6, the range of linearity of pressure with respect to α depends on the temperature. For higher temperature ($k_BT \geqslant 0.01$) the deviation from the linear behavior starts from $\alpha > 0.25$. Therefore, in all our subsequent results, we restrict our simulations to the values of α that maintain thermodynamical consistency.

TABLE II. Slope of pressure from simulation and analytical calculations for different temperatures.

k_BT	Slope (simulation)	Slope (analytic)
0.001	0.057	0.083
0.006	0.350	0.502
0.010	0.575	0.837

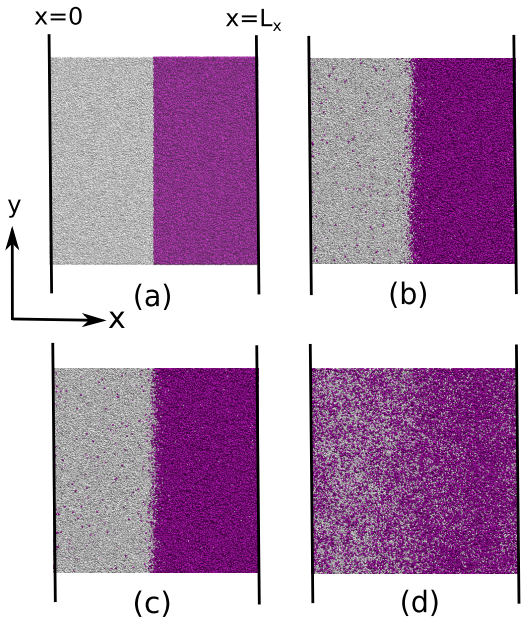

FIG. 7. Snapshots showing the variation of interfacial width formed by phase separating fluids at various temperatures. (a) Initial state at time t=0; (b)–(d) are at time $t = 30000$ for $k_BT = 0.005$, 0.01, and 0.08, respectively with $\alpha = 0.2$.

C. Interfacial width

To further establish our model, we study the stability of the interface between the two-phase separating fluids. The two halves of the simulation box are filled with the two different fluid species at time $t = 0$ [A particles have coordinates from (0,0,0) to $(L_x/2, L_y, L_z)$, and B particles have coordinates from $(L_x/2, L_y, L_z)$ to (L_x, L_y, L_z)]. This creates an initial sharp interface along the x direction, which completely divides the two-phase domains [see Fig. 7(a)]. Periodic boundary conditions are applied in both y and z directions, and a bounce-back reflection condition is applied along the x direction at both ends of the box. The interface then evolves with time, and its advancement depends on the temperature and repulsive parameters. Figures 7(b)–7(d) show the late time interface for different temperatures.

Figure 7 depicts the broadening of the interface with increasing temperature. To quantify this observation from the snapshots, we calculate the density profile of different solvent species and extract the value of the interfacial width. The averaged normalized density is given as

$$\langle \psi_\beta(x) \rangle = \frac{\rho_\beta(x) - \rho_{\beta^*}(x)}{\rho}, \tag{20}$$

where β and β^* represent the two different solvent species. $\rho_\beta(x)$ is the average density of species β ($= A$ or B) in a cell-centered at x with dimension $a \times L_y \times L_z$. Figure 8 shows

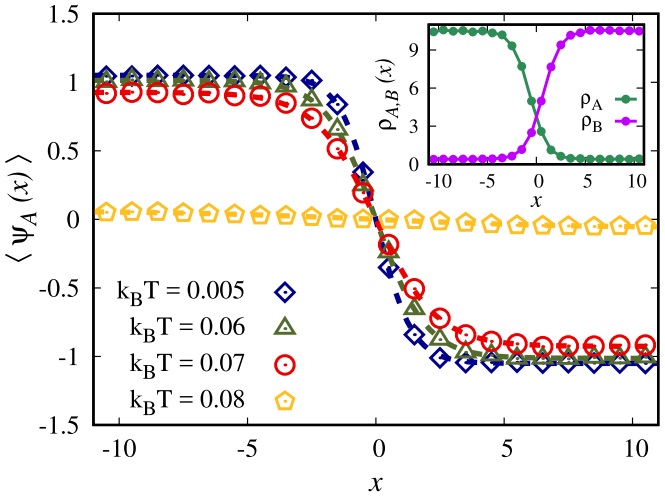

FIG. 8. Normalized density profile as a function of x for different temperatures $k_BT = 0.005, 0.06, 0.07$, and 0.08 with $\alpha = 0.2$. The dashed line is a fit following Eq. (21). The inset plot is the density of A and B particles averaged over cells as a function of distance from the interface at temperature $k_BT = 0.06$ and $\alpha = 0.2$.

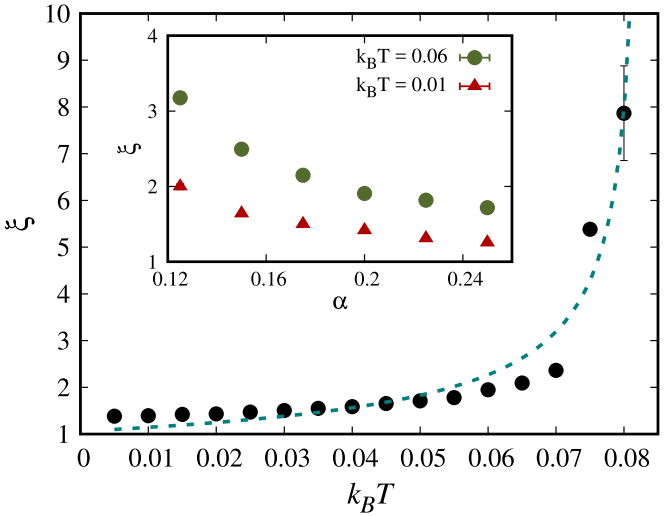

FIG. 9. Variation of interfacial width ξ with respect to temperature for $\alpha = 0.2$. The inset shows the variation of interfacial width with respect to repulsive parameter α for temperatures $k_BT = 0.01$ and 0.06.

the variation of $\langle\psi_A(x)\rangle$ for different temperatures $k_BT = 0.005, 0.06, 0.07$, and 0.08. At lower temperature $k_BT = 0.005$ we observe a sharp fall for $\langle\psi_A(x)\rangle$ indicating a very narrow width of the interface. The width increases as we move toward higher temperatures with the lowered saturation values indicating the mixing of the A and B particles. The inset of Fig. 8 further provides the complete picture of the average density of both A and B species as a function of the distance from the interface.

Within the framework of the Landau theory, the interfacial width can be calculated by fitting the average normalized density profile with the following function [21,34,51]:

$$\langle\psi_\beta(x)\rangle = \psi_{\beta 0}\,\tanh\left(\frac{x}{\xi}\right), \tag{21}$$

where ξ is the interfacial width and $\psi_{\beta 0}$ is the normalized bulk density. The dashed lines in Fig. 8 represent fitting curves using Eq. (21) to evaluate the interfacial width, ξ. Figure 8 shows a good agreement between the density profile observed in our simulation, and the Landau theory given in Eq. (21).

Further, the impact of temperature on the interfacial width is shown in Fig. 9. Higher interfacial width with increasing temperature can be attributed to the dominating entropic interaction among the particles. For a two-fluid interface with a fluctuating concentration, the influence of temperature on the interface width can be roughly calculated using the classical Ising model as follows:

$$\xi \sim \frac{1}{(T_c - T)^\nu}, \tag{22}$$

where T_c is the critical temperature for interface formation. We fit Eq. (22) to our simulation data in Fig. 9. From the fitting with our interfacial width calculation, we find our consolute temperature $T_c \approx 0.08$ and $\nu \approx 0.58$, which is close to the expected value of 0.5 suggested by the Ginzburg-Landau theory [21]. However, when the interface is large, the finite size effect may creep in and the exact value of the consolute temperature may vary keeping the overall behavior the same. The interfacial width is also expected to show variation with respect to the repulsive parameter α. For smaller values of α, the thermal fluctuation wins over the repulsive interaction between A and B particles forming a larger interfacial width. However, the higher values of α tend to overcome the thermal fluctuation giving rise to a sharp interface. In the inset of Fig. 9, the saturation in the value of ξ at given k_BT upon increasing α indicates that there exists a limit in the repulsion parameter, beyond which increasing α will not result in any significant change in interface. Such correlation of our simulation data with the theoretical predictions demonstrates the correctness of our model.

D. Domain coarsening

The time evolution of the phase separation can be quantified by the growth dynamics of the domains upon quenching the mixture at an appropriate temperature so that the two components of the mixture separate out. Typically, the time evolution of the domain radius $R(t)$ follows a power law behavior as

$$R(t) \sim t^\gamma, \tag{23}$$

where γ is the growth exponent which depends on a variety of parameters and constraints [9,34]. For percolating morphology in three dimensions, the growth exponent γ varies with time as the phase separation progresses through different mechanisms [9,48]. It has been shown that, during the early time, $\gamma \sim 1/3$ as the domain growth mostly occurs due to the diffusive transport of the mass flux. However, at late times, the mass transport along the domain boundary happens rapidly by advection which is known as the "viscous hydrodynamics regime" where the interfacial free energy density balances the viscous stress leading to $\gamma \sim 1$. At sufficiently late times, the growth exponent γ is found to be $2/3$ by balancing the

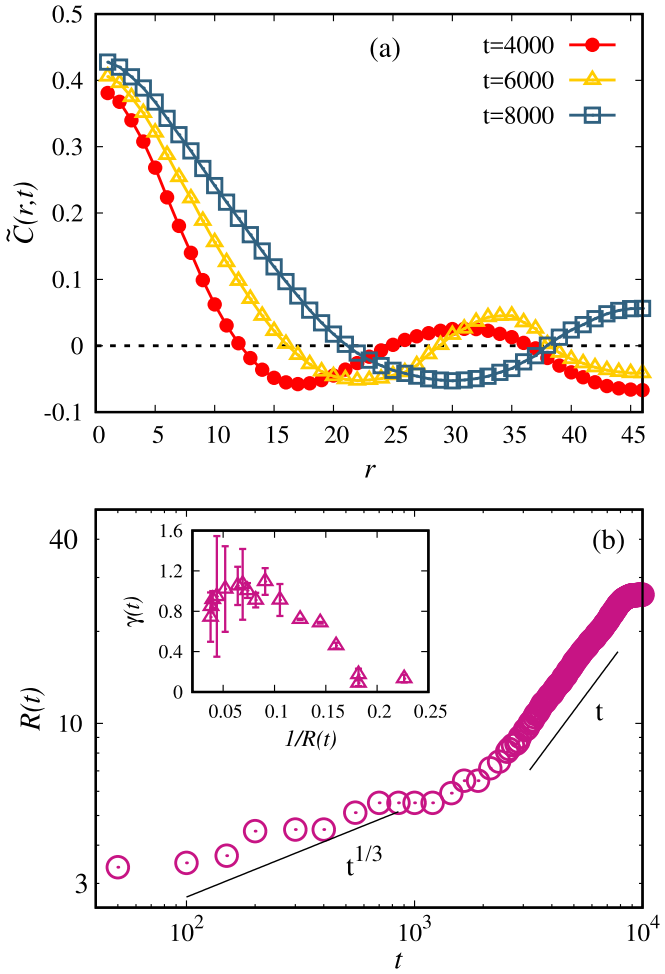

FIG. 10. (a) Correlation function as a function of r for temperature $k_BT = 0.05$ in different simulation times. (b) Variation of average domain radius $R(t)$ with respect to time for $k_BT = 0.05$ on log-log scale. The inset plot shows the variation of instantaneous growth exponent $\gamma(t)$ with the inverse of domain radius. Simulation box size is $52a \times 52a \times 52a$, and $\alpha = 0.2$.

interfacial energy density with kinetic energy density which is known as the "inertial hydrodynamic regime" [9,48].

In our simulation, we calculate the average domain radius $R(t)$ as the distance r at which the spatial correlation function $\tilde{C}(r,t)$ becomes zero for the first time, i.e., $R(t) = \min[r\,\forall\,\tilde{C}(r,t)] = 0$. Here,

$$\tilde{C}(r,t) = \left\langle \psi_\beta^{\chi}(t)\psi_\beta^{\chi'}(t)\right\rangle_{\chi,\chi'}, \tag{24}$$

where $r = |\mathbf{r}_\chi - \mathbf{r}_{\chi'}|$ is the distance between the center of cells χ and χ'. $\langle\ldots\rangle_{\chi,\chi'}$ is the spatial average taken over the pair of cells represented by χ and χ' which are at r distance apart. Figure 10(a) shows the correlation function $\tilde{C}(r,t)$ at different times for the binary system with $k_BT = 0.05$ and $\alpha = 0.2$. At a particular instant t, the distance r at which $\tilde{C}(r,t)$ reaches zero for the first time (indicating the presence of phase boundary) tells us about the average domain radius $R(t)$. The slower decay of $\tilde{C}(r,t)$ with increasing time indicates the increase in the domain radius with time. In Fig. 10(b), we show the time evolution of the average domain radius $R(t)$ at a particular temperature. For $t < 3000$, $R(t) \propto t^{1/3}$, i.e., $\gamma \sim 1/3$ and beyond that $R(t) \propto t$, i.e., $\gamma \sim 1$. The exponent $\gamma \sim 1/3$ can be interpreted as the domain growth mediated by diffusion while $\gamma \sim 1$ highlights the presence of hydrodynamics.

To further substantiate this growth exponent, we calculate the instantaneous growth exponent $\gamma(t)$ as [52]

$$\gamma(t) = \frac{d\ln(R(t))}{d\ln(t)}. \tag{25}$$

The inset of Fig. 10(b) shows the instantaneous exponent as a function of the inverse of domain radius. For $\frac{1}{R(t)} \to 0$, $\gamma(t) \to 1$ before the finite size effect sets in. This shows that at late times, $3000 < t < 9000$, the growth exponent tends to one, which is theoretically expected for the viscous hydrodynamic regime. Hence, our model successfully captures the theoretical predictions of domain coarsening. Within the range of temperatures where the phase separation is observed (see the phase diagram in Fig. 5), the domain growth slows down on decreasing the temperature and a similar trend is also observed for α.

IV. CONCLUSIONS

In this study, we have developed a model for the phase separation of the binary fluid mixture in three dimensions by augmenting the rules of MPC dynamics. With appropriate modification, the proposed model enables the MPCD technique (initially designed for ideal fluids) to simulate nonideal fluids. The model is thermodynamically consistent within a reasonably extensive range of temperature and model parameters. The model was further quantified by investigating the stability of the interface and interfacial width during phase separation. For the explored range of parameters, our results match reasonably well with the theoretical predictions in the literature. Because of its coarse-grained nature, the model is suitable for studying relatively large lengths and time scales. Further, the numerical implementation of the model is relatively easier than the previously developed 3D MPCD model for the phase separation [21,34], and our detailed analysis of phase separation makes the model more approachable.

The developed model can be deployed to study a wide range of phenomena in complex fluids. The approach is advantageous for studying the dynamics of a single or collection of active or passive colloidal particles in a phase-separating medium. This will also help us comprehend unanswered questions in experiments that deal with colloidal motion in phase-separating mixtures [38,39]. The model can be extended easily to explore the effect of wetting and walls during phase separation process.

ACKNOWLEDGMENTS

The authors would like to acknowledge the HPC facility at IISER Bhopal for all the computational work. S.J. thanks UGC, India for providing the research fellowship. The work was supported by the Science and Engineering Research Board, India [Grant No. CRG/2022/003778].

[1] S. Alberti, Phase separation in biology, Curr. Biol. **27**, R1097 (2017).

[2] A. A. Hyman, C. A. Weber and F. Jülicher, Liquid-liquid phase separation in biology, Annu. Rev. Cell Dev. Biol. **30**, 39 (2014).

[3] H. Tanaka and Y. Nishikawa, Viscoelastic Phase Separation of Protein Solutions, Phys. Rev. Lett. **95**, 078103 (2005).

[4] S. Tanaka, M. Ataka, and K. Ito, Pattern formation and coarsening during metastable phase separation in lysozyme solutions, Phys. Rev. E **65**, 051804 (2002).

[5] G. S. Redner, M. F. Hagan, and A. Baskaran, Structure and Dynamics of a Phase-Separating Active Colloidal Fluid, Phys. Rev. Lett. **110**, 055701 (2013).

[6] A. Matsuyama and R. Hirashima, Phase separations in liquid crystal-colloid mixtures, J. Chem. Phys. **128**, 044907 (2008).

[7] H. Benabdelhalim and D. Brutin, Phase separation and spreading dynamics of french vinaigrette, Phys. Fluids **34**, 012120 (2022).

[8] C.-C. Chueh, A. Bertei, and R. Mauri, Dynamics of phase separation of sheared inertialess binary mixtures, Phys. Fluids **32**, 023307 (2020).

[9] A. J. Bray, Theory of phase-ordering kinetics, Adv. Phys. **51**, 481 (2002).

[10] J. A. Thomson, P. Schurtenberger, G. M. Thurston, and G. B. Benedek, Binary liquid phase separation and critical phenomena in a protein/water solution, Proc. Natl. Acad. Sci. USA **84**, 7079 (1987).

[11] Z. Ding, D. Liu, K. Zhao, and Y. Han, Optimizing morphology to trade off charge transport and mechanical properties of stretchable conjugated polymer films, Macromolecules **54**, 3907 (2021).

[12] Y. Xu, M. Mazzawi, K. Chen, L. Sun, and P. L. Dubin, Protein purification by polyelectrolyte coacervation: influence of protein charge anisotropy on selectivity, Biomacromolecules **12**, 1512 (2011).

[13] D. Carati and R. Lefever, Chemical freezing of phase separation in immiscible binary mixtures, Phys. Rev. E **56**, 3127 (1997).

[14] D. Zhou, P. Zhang, and W. E, Modified models of polymer phase separation, Phys. Rev. E **73**, 061801 (2006).

[15] S. Ahmad, S. K. Das, and S. Puri, Crossover in growth laws for phase-separating binary fluids: Molecular dynamics simulations, Phys. Rev. E **85**, 031140 (2012).

[16] L.-S. Luo and S. S. Girimaji, Lattice Boltzmann model for binary mixtures, Phys. Rev. E **66**, 035301(R) (2002).

[17] E. Orlandini, M. R. Swift, and J. M. Yeomans, A lattice Boltzmann model of binary-fluid mixtures, Europhys. Lett. **32**, 463 (1995).

[18] P. V. Coveney and K. E. Novik, Computer simulations of domain growth and phase separation in two-dimensional binary immiscible fluids using dissipative particle dynamics, Phys. Rev. E **54**, 5134 (1996).

[19] P. B. Warren, Hydrodynamic Bubble Coarsening in Off-Critical Vapor-Liquid Phase Separation, Phys. Rev. Lett. **87**, 225702 (2001).

[20] E. Tüzel, G. Pan, T. Ihle, and D. M. Kroll, Mesoscopic model for the fluctuating hydrodynamics of binary and ternary mixtures, Europhys. Lett. **80**, 40010 (2007).

[21] T. Eisenstecken, R. Hornung, R. G. Winkler, and G. Gompper, Hydrodynamics of binary-fluid mixtures—an augmented multiparticle collison dynamics approach, Europhys. Lett. **121**, 24003 (2018).

[22] X. Shan and H. Chen, Lattice Boltzmann model for simulating flows with multiple phases and components, Phys. Rev. E **47**, 1815 (1993).

[23] P. V. Coveney and P. Español, Dissipative particle dynamics for interacting multicomponent systems, J. Phys. A: Math. Gen. **30**, 779 (1997).

[24] J. T. Padding and A. A. Louis, Hydrodynamic and Brownian Fluctuations in Sedimenting Suspensions, Phys. Rev. Lett. **93**, 220601 (2004).

[25] A. Malevanets and R. Kapral, Solute molecular dynamics in a mesoscale solvent, J. Chem. Phys. **112**, 7260 (2000).

[26] K. Mussawisade, M. Ripoll, R. G. Winkler, and G. Gompper, Dynamics of polymers in a particle-based mesoscopic solvent, J. Chem. Phys. **123**, 144905 (2005).

[27] N. Jain and S. Thakur, Collapse dynamics of chemically active flexible polymer, Macromolecules **55**, 2375 (2022).

[28] C. Echeverria and R. Kapral, Molecular crowding and protein enzymatic dynamics, Phys. Chem. Chem. Phys. **14**, 6755 (2012).

[29] P. Chuphal, V. P, and S. Thakur, Dynamics of diffusiophoretic vesicle under external shear flow, J. Chem. Phys. **151**, 064901 (2019).

[30] H. Noguchi and G. Gompper, Dynamics of fluid vesicles in shear flow: Effect of membrane viscosity and thermal fluctuations, Phys. Rev. E **72**, 011901 (2005).

[31] S. Sahoo, Sunil P. Singh, and S. Thakur, Role of viscoelasticity on the dynamics and aggregation of chemically active spheredimers, Phys. Fluids **33**, 017120 (2021).

[32] T. Yu, P. Chuphal, S. Thakur, S. Y. Reigh, D. P. Singh, and P. Fischer, Chemical micromotors self-assemble and self-propel by spontaneous symmetry breaking, Chem. Commun. **54**, 11933 (2018).

[33] A. Zöttl and H. Stark, Hydrodynamics Determines Collective Motion and Phase Behavior of Active Colloids in Quasi-Two-Dimensional Confinement, Phys. Rev. Lett. **112**, 118101 (2014).

[34] C. Echeverria, K. Tucci, O. Alvarez-Llamoza, E. O. Guillén, M. Morales-Rodríguez, and M. Cosenza, Mesoscopic model for binary fluids, Front. Phys. **12**, 128703 (2017).

[35] T. Ihle and E. Tüzel, Static and dynamic properties of a particle-based algorithm for non-ideal fluids and binary mixtures, Prog. Comput. Fluid Dyn. **8**, 138 (2008).

[36] A. Montessori, M. Lauricella, A. Tiribocchi, F. Bonaccorso, and S. Succi, Multiparticle collision dynamics for fluid interfaces with near-contact interactions, J. Chem. Phys. **152**, 144101 (2020).

[37] Z. Tan, V. Calandrini, J. K. G. Dhont, G. Nägele, and R. G. Winkler, Hydrodynamics of immiscible binary fluids with viscosity contrast: a multiparticle collision dynamics approach, Soft Matter **17**, 7978 (2021).

[38] I. Buttinoni, J. Bialké, F. Kümmel, H. Löwen, C. Bechinger, and T. Speck, Dynamical Clustering and Phase Separation in Suspensions of Self-Propelled Colloidal Particles, Phys. Rev. Lett. **110**, 238301 (2013).

[39] E. F. Semeraro, R. Dattani, and T. Narayanan, Microstructure and dynamics of Janus particles in a phase separating medium, J. Chem. Phys. **148**, 014904 (2018).

[40] T. Sakai, Y. Chen, and H. Ohashi, Real-coded lattice gas model for ternary amphiphilic fluids, Phys. Rev. E **65**, 031503 (2002).

[41] R. Kapral, *Multiparticle Collision Dynamics: Simulation of Complex Systems on Mesoscales* (John Wiley & Sons, Ltd, 2008).

[42] M. Laradji, S. Toxvaerd, and O. G. Mouritsen, Molecular Dynamics Simulation of Spinodal Decomposition in Three-Dimensional Binary Fluids, Phys. Rev. Lett. **77**, 2253 (1996).

[43] A. J. Archer and N. B. Wilding, Phase behavior of a fluid with competing attractive and repulsive interactions, Phys. Rev. E **76**, 031501 (2007).

[44] T. Ihle, E. Tüzel, and D. M. Kroll, Consistent particle-based algorithm with a non-ideal equation of state, Europhys. Lett. **73**, 664 (2006).

[45] E. Tüzel, T. Ihle, and D. M. Kroll, Constructing thermodynamically consistent models with a non-ideal equation of state, Math. Comput. Simul. **72**, 232 (2006).

[46] A. W. Zantop and H. Stark, Multi-particle collision dynamics with a non-ideal equation of state. I, J. Chem. Phys. **154**, 024105 (2021).

[47] T. Ihle and D. M. Kroll, Stochastic rotation dynamics: A galilean-invariant mesoscopic model for fluid flow, Phys. Rev. E **63**, 020201(R) (2001).

[48] S. Puri and V. Wadhawan, *Kinetics of phase transitions* (Taylor & Francis, 2009).

[49] H. Tanaka, A new coarsening mechanism of droplet spinodal decomposition, J. Chem. Phys. **103**, 2361 (1995).

[50] T. Ihle, E. Tüzel, and D. M. Kroll, Resummed green-kubo relations for a fluctuating fluid-particle model, Phys. Rev. E, **70**, 035701 (2004).

[51] S. A. Safran, *Statistical Thermodynamics Of Surfaces, Interfaces, And Membranes*, 1st ed. (CRC Press, 2003).

[52] D. A. Huse, Corrections to late-stage behavior in spinodal decomposition: Lifshitz-Slyozov scaling and Monte Carlo simulations, Phys. Rev. B **34**, 7845 (1986).